Invited paper

OPTO-ELECTRONICS REVIEW **10**(4), 271–286 (2002)

AlGaN and InAlGaN alloys – epitaxial growth, optical and electrical properties, and applications

H.X. JIANG* and J.Y. LIN

Department of Physics, Kansas State University, Manhattan, KS 66506-2601, USA

The paper summarises some of recent advances made by the author's group on the growth, characterization and applications of AlGaN and InAlGaN alloys. Electrical, optical as well as optoelectronic properties have been studied. It is shown that the effect of carrier localisation in undoped AlGaN alloys enhances with increased Al contents and is related to the insulating nature of AlGaN of high Al contents. Si-doping reduces the effect of carrier localization in AlGaN alloys and a sharp increase in conductivity occurs when the Si doping concentration increases to above 10^{18} cm^{-3}. For the Mg-doped $Al_xGa_{1-x}N$ alloys, p-type conduction was achieved for x up to 0.27. Due to the strong piezoelectric polarization and deep triangular potential notch in $Al_xGa_{1-x}N$ (x = 0.5) heterointerface, a total of five emission lines related with the two-dimensional electron gas in heterostructure have been observed, which correspond to the recombination between the electrons from different sub-bands. The dominant optical transition at low temperatures in $In_xAlyGa_{1-x}N$ quaternary alloys is due to localized exciton recombination, while the localisation effects were combined from those of InGaN and AlGaN ternary alloys with comparable In and Al compositions. Finally micro-size ultraviolet light emitters are demonstrated.

Keywords: AlGaN alloys, InAlGaN alloys, AlN epilayers, light emitters, time-resolved photoluminescence.

1. Background

III-nitride wide bandgap semiconductors, with energy band gap varying from 0.8 eV (InN) to 3.4 eV (GaN) to about 6.2 eV (AlN), have been recognised as technologically important materials [1–10]. Photonic devices based on III-nitrides offer benefits including UV/blue emission, large band offsets of GaN/AlN or InN/AlN heterostructures allowing novel quantum well (QW) device design, and inherently high emission efficiencies. Furthermore, electronic devices based on III-nitride heterostructures, including heterojunction field effect transistors (HFETs) and bipolar transistors (HBTs), have great promises in microwave and millimeter-wave electronic device applications, due to the high peak electron velocity, high saturation velocity, high breakdown voltage, low noise, and thermal stability of the system. III-nitride based optoelectronic and electronic devices may operate at much higher temperatures and voltages/power levels for any dimensional configuration and in harsher environments than other semiconductor devices and are expected to provide much lower temperature sensitivities, which are crucial advantages for many applications.

Although tremendous progress has been made for III-nitrides research and development in terms of both fundamental understanding as well as devices applications, the materials we understand relatively well today is just GaN compound and In (Al) GaN alloys with In (Al) content less than 30% (50%). InGaN alloys with high In contents (50%), which emit light in the orange to red colour spectral range, can be replaced by other semiconductors. However, AlGaN alloys with high Al contents, covering from 350 nm to 200 nm, cannot be replaced by any other semiconductor system due to the fact that no other semiconductors possess such a large direct bandgap (diamond is 5.4 eV with indirect bandgap) as well as the ability of bandgap engineering through the use of III-nitride heterostructures.

There is currently a great need of solid-state ultraviolet (UV) emitters for detection of chemical and biological agents as well as for general lighting. In such applications based on III-nitride wide bandgap semiconductors, conductive n-type and p-type AlGaN or InAlGaN alloys with high Al contents are indispensable. The use of high Al-content AlGaN layer is also expected to increase the overall figure of merit of the AlGaN/GaN HFETs due to the combined advantages of enhanced band offset, lattice mismatch-induced piezoelectric effect, and the electron velocity in the two dimensional electron gas (2DEG) channel. Thus improving the material quality of high Al content AlGaN alloys is also of crucial importance for fabricating high performance AlGaN/GaN HFETs.

This paper summarises some of the recent advances made by the authors' group on the growth, characterization and applications of AlGaN and InAlGaN alloys. It was shown that the effect of carrier localisation in undoped AlGaN alloys enhances with increased Al contents and is

*e-mail: jiang@phys.ksu.edu

related to the insulating nature of AlGaN of high Al contents. It was also shown that $Al_xGa_{1-x}N$ alloys could be made n-type for x up to 1 (pure AlN). Time-resolved photoluminescence (PL) studies carried out on these materials have revealed that Si-doping reduces the effect of carrier localization in $Al_xGa_{1-x}N$ alloys and a sharp drop in carrier localisation energy as well as a sharp increase in conductivity occurs when the Si doping concentration increases to above 1×10^{18} cm^{-3}. For the Mg-doped $Al_xGa_{1-x}N$ alloys, p-type conduction was achieved for x up to 0.27. From the Mg acceptor activation energy as a function of Al content, the resistivity of Mg-doped $Al_xGa_{1-x}N$ with high Al contents can be estimated. For example, the projected resistivity of $Al_xGa_{1-x}N$ (x = 0.45) is around 2.2×10^4 Ω cm. Thus, alternative methods for acceptor activation in AlGaN or InAlGaN with high Al contents must be developed before the high performance deep UV emitters can be realised.

The optical properties of AlGaN/GaN heterostructures with high Al content were also studied. Due to the strong piezoelectric polarisation and deep triangular potential notch in $Al_xGa_{1-x}N$/GaN (x = 0.5) heterointerface, a total of five emission lines related with the 2DEG in $Al_xGa_{1-x}N$/ GaN (x = 0.5) heterostructure have been observed, which correspond to the recombination between the electrons from different sub-bands (n = 1 to 5) in the conduction band and the photoexcited holes in the valence band. The 2DEG PL emission lines were found to be observable at temperatures as high as 220 K, in sharp contrast to the AlGaAs/GaAs heterostructures system in which the 2DEG emission lines were observable only at low temperatures (T <20 K).

Optoelectronic properties of InAlGaN quaternary alloys were studied. It was observed that the dominant optical transition at low temperatures in $In_xAl_yGa_{1-x}N$ quaternary alloys was due to localized exciton recombination, while the localisation effects in $In_xAl_yGa_{1-x}N$ quaternary alloys were combined from those of InGaN and AlGaN ternary alloys with comparable In and Al compositions. Our studies have revealed that $In_xAl_yGa_{1-x}N$ quaternary alloys with lattice matched with GaN epilayers (y ~4.8x) have the highest optical quality. The quantum efficiency of $In_xAl_yGa_{1-x}N$ quaternary alloys was also enhanced significantly over AlGaN alloys with a comparable Al content. It was also found that the responsivity of the $In_xAl_yGa_{1-x-y}N$ quaternary alloy photodetectors exceeded that of AlGaN alloy of comparable cut-off wavelength by a factor of five. The AlGaN ternary and InAlGaN quaternary were incorporated into UV (340 nm) emitter structures. The operation of 340 nm micro-size UV emitters have been demonstrated.

AlN epilayers with high optical qualities have also been grown on sapphire substrates. Very efficient band-edge PL emission lines have been observed for the first time with above bandgap deep UV laser excitation. We have shown that the thermal quenching of the PL emission intensity is much less severe in AlN than in GaN and the optical quality of AlN can be as good as GaN.

2. Experimental

$Al_xGa_{1-x}N$ alloys and AlN epilayers (1 μm thick) were grown on sapphire (0001) substrates with AlN buffer layers by metal organic chemical vapour deposition (MOCVD). The growth temperature and pressure were around 1050°C and 50 Torr, respectively. The metal organic sources used were trimethylgallium (TMGa) for Ga and trimethylaluminum (TMAl) for Al. For Mg-doping of AlGaN, bis-cyclopentadienyl-magnesium (Cp_2Mg) was transported into the growth chamber with ammonia during growth. The gas sources used were blue ammonia (NH_3) for N and Silane (SiH_4) for Si doping and the doping level was varied by controlling the SiH_4 flow rate. The Al contents of $Al_xGa_{1-x}N$ alloys were determined by energy dispersive x-ray (EDX) microanalysis and x-ray diffraction (XRD) measurement as well as by the flow rates of TMGa and TMAl. The Al contents (x) determined by all three methods agreed within ±0.02. The Si-dopant concentrations were determined by the flow rate of SiH_4 as well as by the variable temperature Hall effect measurement at elevated temperatures (T < 650 K). Additionally, secondary ion mass spectroscopy (SIMS) measurements were performed (by Charles and Evan) for selective samples to verify the Si-dopant concentrations. Atomic force microscopy (AFM) and scanning electron microscopy (SEM) were employed to examine the surfaces and revealed crack-free $Al_xGa_{1-x}N$ epilayers. Variable temperature Hall-effect (standard Van der Pauw) measurements were employed to measure the electron concentration, mobility, and resistivity of these materials.

To investigate the optical properties of $Al_xGa_{1-x}N$/GaN heterostructures with high Al contents, we have targeted for x = 0.5. A set of $Al_{0.5}Ga_{0.5}N$/GaN heterostructure samples was grown on sapphire (0001) substrates with GaN buffer layers. These samples consist of a 1 μm-thick undoped GaN epilayer, followed by a 5 Å-thick undoped $Al_{0.5}Ga_{0.5}N$ spacer layer, again followed by the top Si-doped $Al_{0.5}Ga_{0.5}N$ layer with varying thickness (d) from 55 to 140 Å. The growth temperature and pressure of the top Si-doped $Al_{0.5}Ga_{0.5}N$ layer were 1060°C and 75 Torr, respectively. The targeted Si doping concentration for the top AlGaN layer was 5×10^{18} cm^{-3}. Atomic force microscopy (AFM) was employed to examine the surfaces of these samples. Variable temperature Hall measurements were used to measure the 2DEG mobility and the sheet carrier density of $Al_{0.5}Ga_{0.5}N$/GaN heterostructures.

For the growth of $In_xAl_yGa_{1-x-y}N$ quaternary alloys, a GaN epilayer of about 1 μm was first deposited on the sapphire substrate with a 25 nm low temperature GaN buffer layer, followed by the deposition of a 0.1 μm $In_xAl_yGa_{1-x-y}N$ epilayer. The growth temperature and pressure for the underneath GaN epilayer were 1050°C and 300 Torr, respectively. The growth temperature and pressure of InAlGaN quaternary alloys varied around 780°C and 300 Torr, respectively. In and Al compositions were

controlled by varying the flow rates of TMIn and TMAl. The actual Al and In contents of $In_xAl_yGa_{1-x-y}N$ quaternary alloys were determined by EDX and SIMS measurements as well as by the flow rates of TMIn and TMAl.

A deep UV (10 mW @ 196 nm) picosecond time-resolved photoluminescence (PL) spectroscopy system was specially designed to probe the optical properties of materials and device structures based on AlGaN and InAlGaN alloys with high Al contents and hence serves as "eyes" for monitoring the material qualities of these materials. The picosecond time-resolved PL spectroscopy system basically consists of a frequency quadrupled 100 femtosecond Ti: sapphire laser with a 76 MHz repetition rate, a monochromator (1.3 m), and a streak camera with a detection capability ranging from 185–800 nm and a time resolution of 2 ps [11]. For GaN-rich alloys, in addition to the 196 nm deep UV laser, a second laser system with excitation wavelength tunable from 285 nm to 320 nm was also used as an excitation source. This second laser system consisted of a cavity-dumped dye laser with 6G dye solutions, which was pumped by a YAG laser with a frequency doubler, while the output of the dye laser was frequency doubled again to provide a tunability from 285–320 nm [11]. This was to check the differences in PL spectral shapes due to the variation in optical absorption depth as a result of the use of different excitation wavelengths. In general, the PL results of GaN-rich alloys obtained by the two laser systems of different excitation wavelengths were similar.

3. Results and discussions

3.1. Time-resolve photoluminescence studies of undoped AlGaN epilayers

Low-temperature (10 K) cw PL spectra of $Al_xGa_{1-x}N$ alloys with x = 0.3, 0.5, and 0.7 are presented in Fig. 1(a) [12]. The PL peak position (E_p), the full width at half maximum (FWHM) as well as integrated intensity (S) are also indicated in the figure. Besides the shift of the peak position towards shorter wavelength with increasing Al-content, one also notices a considerable decrease in the PL intensity and increase in the full width at half maximum (FWHM), which is caused by the reduction in crystalline quality as well as alloy broadening. The solid lines are the least-squares fits of data with two peaks of Gaussian distributions. With longitudinal optical (LO) phonon energies around 112 and 92 meV for AlN and GaN, respectively [13], the low energy shoulders in Fig. 1(a) are assigned to LO phonon replica of the main emission peak. An efficient way to investigate the quality of semiconductor alloy systems is by studying the linewidths of their excitonic photoluminescence spectra at low temperatures. Theoretically, higher is the quality of the alloy; closer are the excitonic photoluminescence linewidths to the theoretically predicted values [14]. It was found that the values of the excitonic linewidths we measured agree very well with those calculated using a model in which the broadening ef-

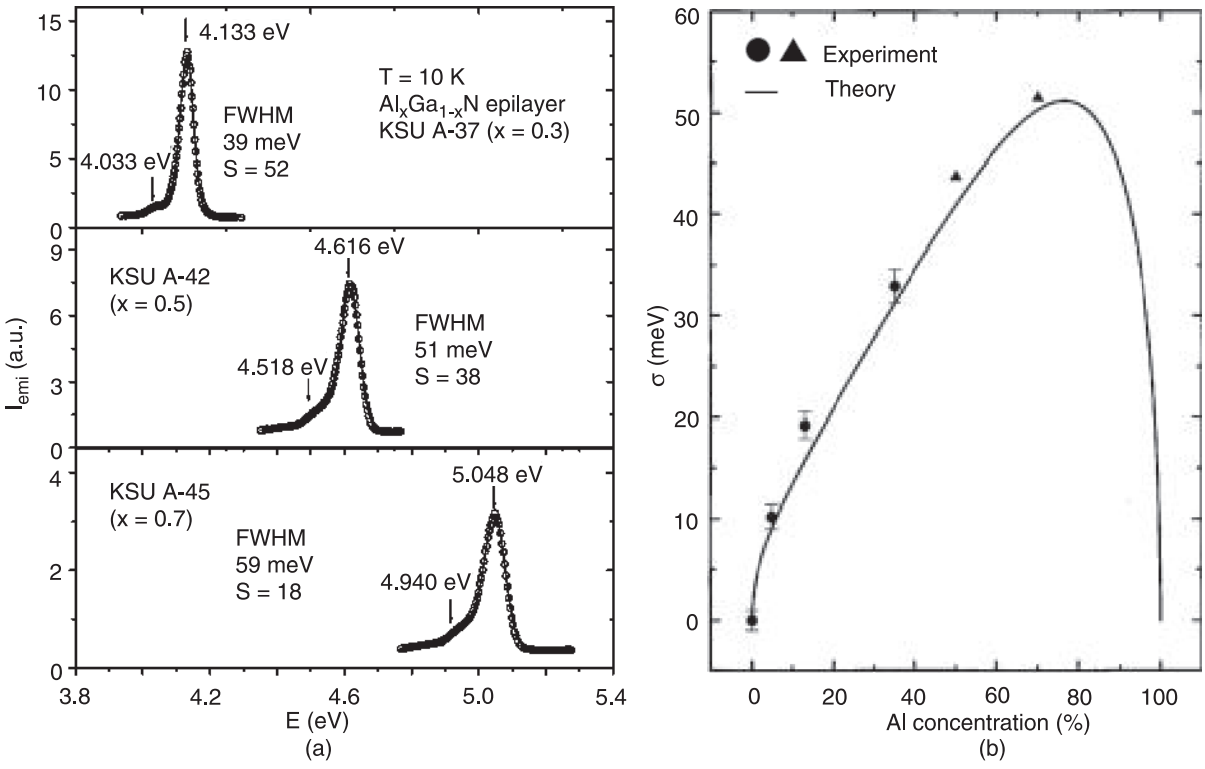

Fig. 1. Photoluminescence spectra of $Al_xGa_{1-x}N$ alloys measured at 10 K for different Al concentrations x = 0.3, 0.5, and 0.7 measured at 10 K (a). Variation of excitonic emission linewidth as a function of Al concentration: theoretical calculation (solid line), determined from the line shape analysis of the PL spectra measured at 10 K (triangles and circles) (b). The constant value of the inhomogeneous broadening at x = 0 has been subtracted from the data, so as to consider only the effect of the compositional disorder (after Refs. 12, 13, and 14).

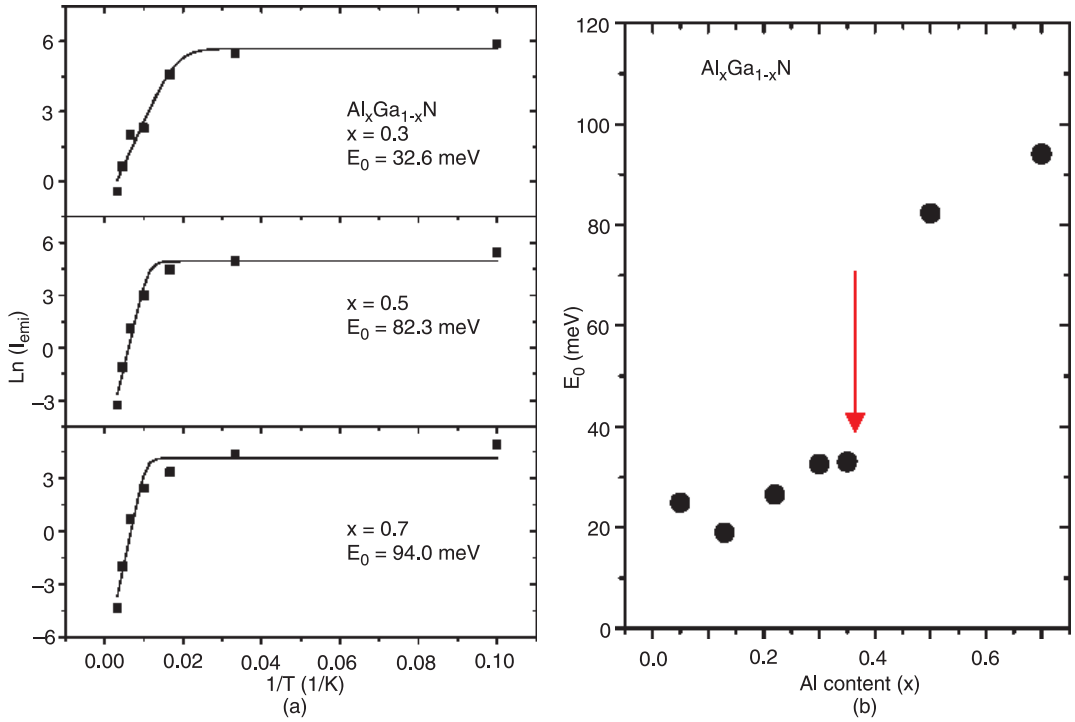

Fig. 2. Arrhenius plots of PL intensity for undoped AlGaN alloys with $x = 0.3$, 0.5, and 0.7 (a). The solid lines are the least squares fit of data with Eq. (1). The fitted activation energy, E_0, is also indicated in the figure. The activation energy E_0 as a function of Al composition x (b). A drastic increase of E_0 is evident at x ~0.4 (after Ref. 12).

fect is assumed to be due to compositional disorder in completely random semiconductor alloys. This is illustrated in Fig 1(b), which displays the variation of the exciton emission linewidth (σ) as a function of Al concentration. We found that the measured values of agree rather well with the calculated values, thus suggesting a high quality of our samples and that random compositional disorder is the main broadening mechanism in AlGaN alloys [14].

Figure 2(a) shows the Arrhenius plots of the PL emission intensity of $Al_xGa_{1-x}N$ alloys with x = 0.3, 0.5, and 0.7. The solid lines are the least squares fit of data with equation

$$I_{emi}(T) = I_0/[1 + C\exp(-E_0/kT)], \qquad (1)$$

where E_0 is the activation energy of the PL emission intensity, which is correlated with the carrier localisation energy induced by compositional disorder. The fitted activation energy E_0 is indicated in the figure. Figure 2(b) plots the Al composition (x) dependence of the activation energy (E_0). The most intriguing result is that E_0 has a sharp increase at x ~0.4. For x 0.5, E_0 is as large as 90 meV and is much larger than the thermal energy at room temperature (25 meV).

Time-resolved PL spectra have been measured at 10 K. Figure 3(a) shows the temporal responses of the PL emissions from AlGaN alloys (with x = 0.3, 0.5, 0.7) measured at their respective spectral peak positions. It clearly shows an increase of decay lifetime with increasing Al content. Figure 3(b) displays the Al composition (x) dependence of the recombination lifetime. It is quite convincing that the

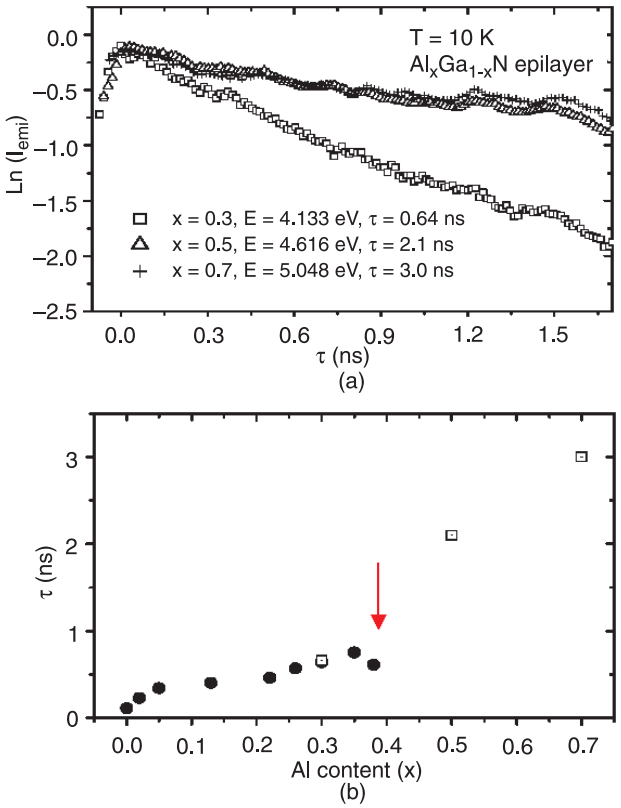

Fig. 3. Temporal responses of the PL emissions from undoped $Al_xGa_{1-x}N$ alloys with x = 0.3, 0.5, and 0.7 measured at 10 K and their emission peak positions (a). The Al content dependence of the measured decay lifetime of $Al_xGa_{1-x}N$ alloys at 10 K (after Ref. 12) (b).

decay lifetime shows exactly the same trend as that of the activation energy of the PL emission intensity. The PL decay lifetime is expected to increase with the carrier/exciton localisation energy [15,16]. There are many important consequences for large E_0 for x greater than 0.4. Larger E_0 implies larger carrier/exciton localisation energies, which we believe accounts partly for the low conductivities of AlGaN alloys of high Al contents – a fact has been known for Al-rich AlGaN alloys for many years [17]. We have measured the conductivity of a set of undoped AlGaN alloys with x between 0.3 and 0.5 and the results are summarized in Table 1. As shown in Table 1, the resistivity increases by about 3 orders of magnitude when Al contents increased from 0.3 to 0.4. It becomes a highly resistive material at x around 0.5 for undoped $Al_xGa_{1-x}N$ alloys. The results shown in Table 1 further corroborate the optical data presented in Figs. 2 and 3.

Our results thus strongly suggested that a sharp increase of the carrier localisation energy in undoped high Al content AlGaN alloys is responsible for all the behaviours reported here. These include sharp increase of (a) PL emission intensity activation energy, (b) PL decay lifetime, and (c) resistivity, for undoped $Al_xGa_{1-x}N$ alloys at x around 0.4.

Table 1. Resistivity vs x in undoped $Al_xGa_{1-x}N$ (after Ref. 12).

Al content x	Resistivity ρ (Ω cm)
0.3	0.18
0.35	2.1
0.4	190
0.45	374
0.5	$>10^5$

3.2. Achieving highly conductive $Al_xGa_{1-x}N$ alloys with high Al contents

We have investigated the MOCVD growth of n-type $Al_xGa_{1-x}N$ alloys by Si-doping [18]. By examining the electrical and optical properties of vast numbers of AlGaN samples grown under different conditions, we concluded that:

(i) the conductivity of $Al_xGa_{1-x}N$ alloys continuously increases with an increase of Si doping level for a fixed value of Al content and

(ii) there exists a critical Si-dopant concentration of about 1×10^{18} cm^{-3} that is needed to convert insulating $Al_xGa_{1-x}N$ alloys with high Al contents (x ≥ 0.4) to n-type.

This is illustrated in Fig. 4, which shows the free electron concentration (n), mobility (μ), conductivity (σ) of Si-doped $Al_xGa_{1-x}N$ alloys as functions of the Si dopant concentration (N_{Si}) for three different Al compositions, x = 0.4, 0.45, and 0.5. The results clearly reveal that there exists a critical Si-dopant concentration for converting insulating $Al_xGa_{1-x}N$ ($x \geq 0.4$) to n-type and the critical dopant concentration is

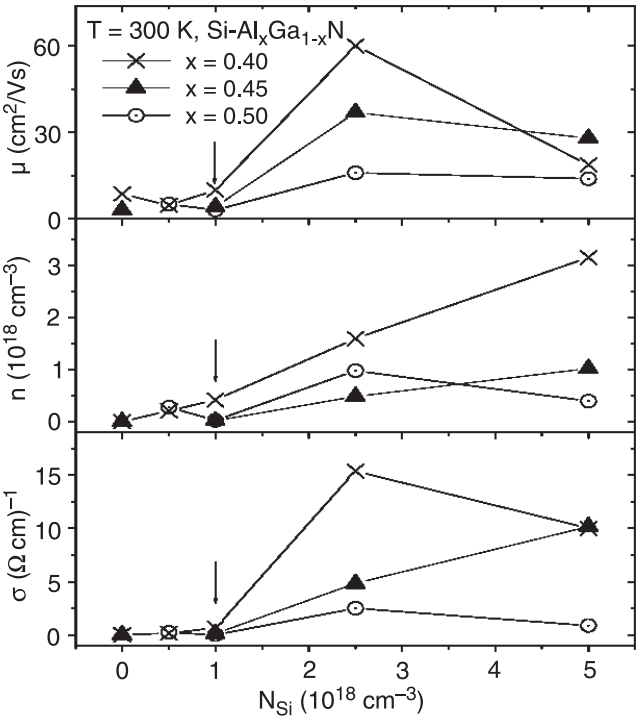

Fig. 4. Mobility (μ), free electron concentration (n), and conductivity (σ) of Si-doped n-type $Al_xGa_{1-x}N$ alloys as functions of the Si dopant concentration (N_{Si}) for three different Al compositions, x = 0.4, 0.45, and 0.5 (after Ref. 18).

about 1×10^{18} cm^{-3}. We believe that this is a direct consequence of electrons filling the localised states in $Al_xGa_{1-x}N$ alloys caused by compositional disorder. Our results thus indicated that the density of the localised states in $Al_xGa_{1-x}N$ alloys with $x \geq 0.4$ below the mobility edge (energy that separates the localised states from the extended states) is on the order of 1×10^{18} cm^{-3}.

Figure 5(a) shows the room-temperature (300 K) PL spectra of $Al_xGa_{1-x}N$ with three different Si doping concentrations (N_{Si}) at fixed Al content x = 0.4, 0.45, and 0.5. In addition to the shift of the peak positions (E_p) toward longer wavelengths at higher doping levels due to the effect of the bandgap renormalisation, we also observe a considerable increase in the PL emission intensity with increasing N_{Si}. The improvement in optical quality by Si doping has been observed previously in GaN epilayers [19–21] and AlGaN/GaN multiple quantum wells [22]. The relative PL intensities for Si-doped $Al_xGa_{1-x}N$ alloys seen here increase by about one order of magnitude when the Si doping concentration is varied from 0 to 5×10^{18} cm^{-3}. For example, for x = 0.45, the relative PL emission intensity increases from 5 to 37 and to 44 as the doping concentration increases from 0 to 1×10^{18} cm^{-3} and to 5×10^{18} cm^{-3}.

We have also measured the carrier localisation energy and recombination lifetime as functions of Si doping for representative n-type $Al_xGa_{1-x}N$ epilayers with different Si doping levels up to 5×10^{18} cm^{-3}, as we have done for the undoped $Al_xGa_{1-x}N$ layers (Figs. 2 and 3). The recombination lifetime and activation energy E_0 of PL emission for

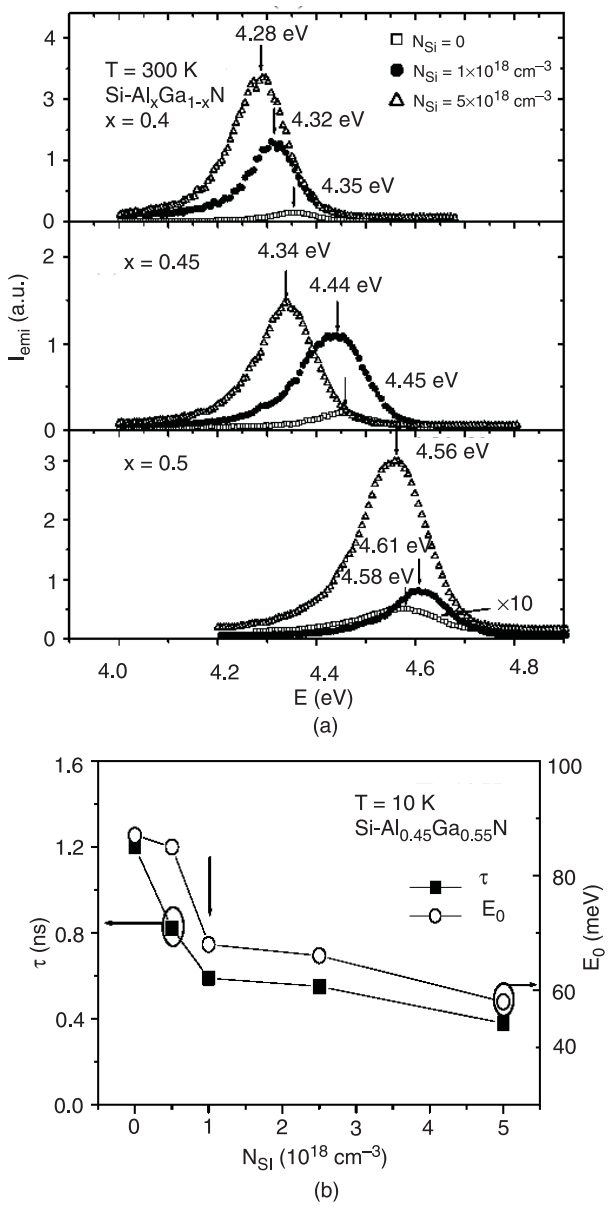

Fig. 5. Room temperature PL spectra of Si-doped n-type $Al_xGa_{1-x}N$ alloys with three different Si dopant concentrations (N_{Si}) for x = 0.4, x = 0.45, and x = 0.5 (a). The Si dopant concentration dependence of the recombination lifetime τ and thermal activation energy E_0 of the PL emission intensity for $Al_{0.45}Ga_{0.55}N$ alloys (after Ref. 18) (b).

Si-doped $Al_{0.45}Ga_{0.55}N$ epilayers as functions of doping level are plotted in Fig. 5(b). Both values of τ and E_0 exhibit initial sharp decreases when the Si doping concentration is increased from N_{Si} = 0 to N_{Si} = 1×10^{18} cm^{-3}, followed by gradual decreases as N_{Si} is further increased. These results suggest that Si-doping reduces the carrier localization effect with a sharp reduction in carrier localisation energy taking place at around N_{Si} = 1×10^{18} cm^{-3}. The results shown in Fig. 5(b) thus corroborate the electrical data presented in Fig. 4. Our results suggest that the critical Si-doping concentration needed to fill up the localized states in $Al_xGa_{1-x}N$ alloys ($x \geq 0.4$) is around

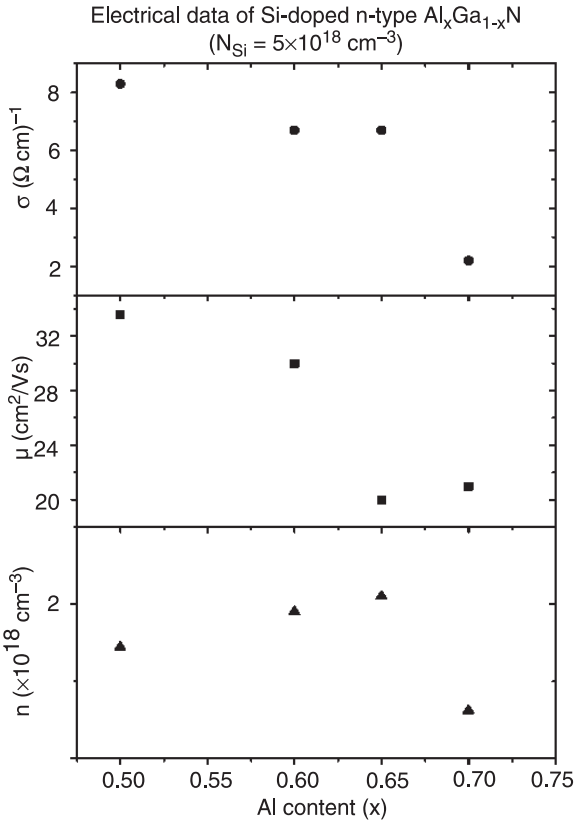

Fig. 6. The free electron concentration (n), mobility (μ), and conductivity (σ) of Si-doped n-type $Al_xGa_{1-x}N$ alloys as functions of the Al content (x) for Si dopant concentration $N_{Si} = 5\times10^{18}$ cm^{-3} (after Ref. 18).

N_{Si} = 1×10^{18} cm^{-3}, above which carriers are able to transport via extended states and reasonable conductivities can be achieved. Therefore in order to obtain good n-type conductivities in $Al_xGa_{1-x}N$ alloys ($x \geq 0.4$), Si doping levels above 1×10^{18} cm^{-3} is required.

Indeed, by fixing the Si dopant concentration at 5×10^{18} cm^{-3} while varying the growth conditions slightly, we have achieved highly conductive $Al_xGa_{1-x}N$ alloys with high Al contents (x up to 0.7) [18]. The Hall data for this new batch of samples are summarised in Fig. 6. Conductivity values of 6.7 Ω^{-1} cm^{-1} and 2.2 Ω^{-1} cm^{-1}, respectively, have been achieved for $Al_{0.65}Ga_{0.35}N$ and $Al_{0.7}Ga_{0.3}N$ alloys. We believe that the n-type conductivity values we have achieved here for $Al_xGa_{1-x}N$ alloys (x up to 0.7) are sufficiently high for deep UV emitter applications.

3.3. Properties of p-type AlGaN epilayers

We have investigated the MOCVD growth and optical and electrical properties of Mg-doped $Al_xGa_{1-x}N$ alloys. Electrical studies have revealed that we have achieved p-type conduction in $Al_xGa_{1-x}N$ epilayers for x up to 0.27 [23]. PL emission lines due to band-to-impurity transitions of free electrons with neutral Mg acceptors in $Al_xGa_{1-x}N$ alloys have been observed, from which the values of the Mg acceptor activation energy E_A were deduced and were found

to increase with an increase of Al content. These were found to match very well with those obtained by Hall measurements.

The Mg-doped p-type $Al_xGa_{1-x}N$ epitaxial layers of thickness 1 μm were grown on sapphire substrates with a 30 nm GaN buffer layers. For Mg-doping, bis-cyclopentadienyl-magnesium (Cp_2Mg) was transported into the growth chamber with ammonia during growth. Postgrowth annealing at 950°C in nitrogen gas ambient for 8 s resulted in p-type conduction, as verified by Hall measurements. A further anneal at 600°C for 2 min in nitrogen gas resulted in the room temperature PL spectra as shown in Fig. 7 for the Mg-doped p-type $Al_xGa_{1-x}N$ for x = 0.22, 0.25 and 0.27. As can be seen, the emission intensities of these spectra decrease with increase in x, a phenomenon that is discussed in section 3.1 and is related to reduction in crystalline quality with increasing x. The emission peaks are observed at 3.615 eV, 3.667 eV and 3.682 eV for x = 0.22, 0.25 and 0.27 respectively, which are greater than the band edge transition of 3.42 eV for GaN. We assign these emission lines to the band-to-impurity transitions for the recombination of free electrons with neutral Mg acceptors in $Al_xGa_{1-x}N$. With the origin of these peaks thus assigned, the activation energy $E_A(x)$ of the ionised Mg impurity in $Al_xGa_{1-x}N$ can be deduced simply by the difference between the energy gap $E_g(x)$ and the observed band-to-impurity emission peak $E(e^-,A^o)$. $E_g(x)$ can be estimated from the expression

$$E_g(x) = (1-x)E_{g,GaN} + xE_{g,AlN} - bx(1-x) \qquad (2)$$

and $E_A(x) = E_g(x) - E(e^-, A^o)$. In the above expression, we use widely accepted value of the energy gap for GaN, $E_{g,GaN}$ = 3.42 eV, for AlN, $E_{g,AlN}$ = 6.20 eV and of the bowing parameter b = 0.90 [24]. With these, E_A values of 0.262 eV, 0.279 eV and 0.311 eV corresponding to Al contents 0.22, 0.25 and 0.27, respectively, are obtained. It is expected that different choices of the bowing parameter b would result in variations in the E_A values. However, because the Mg acceptor level in AlGaN alloys is quite deep, the uncertainties in E_A values due to different choices of b are not very significant. For example, the above optically determined E_A values from Eq. (2) will be reduced by about 17–20 meV if the bowing parameter b = 1 is used. The value of E_A we obtained in the above manner are plotted as a function of Al content x in Fig. 8, together with those reported previously [25,26], all obtained by means of variable temperature Hall measurements.

Also shown in this figure are data points for p-GaN and for p-$Al_{0.27}Ga_{0.73}N$ where we determined E_A by variable temperature Hall measurements (0.15 eV and 0.309 eV respectively). The measured temperature dependence of Hall

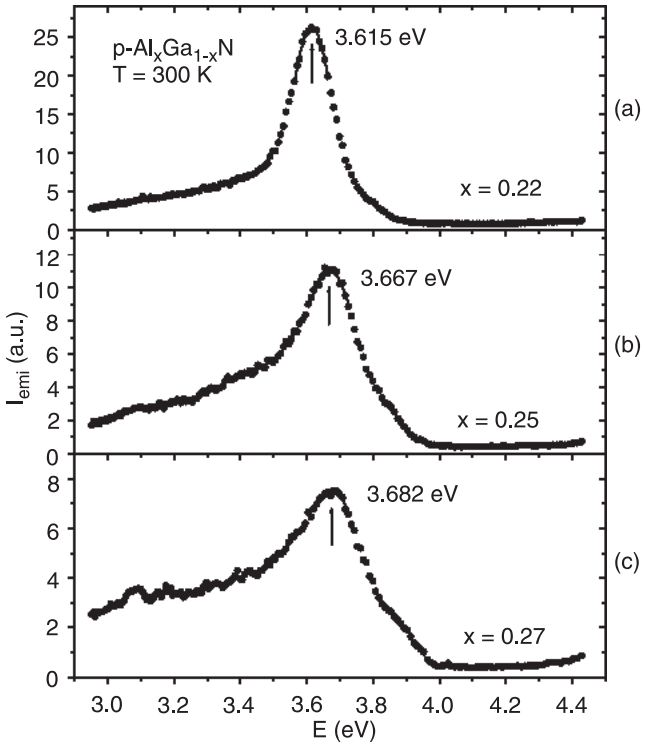

Fig. 7. Room temperature cw PL spectra from Mg-doped p-type $Al_xGa_{1-x}N$ for (a) x = 0.22, (b) x = 0.25 and (c) x = 0.27 (after Ref. 23).

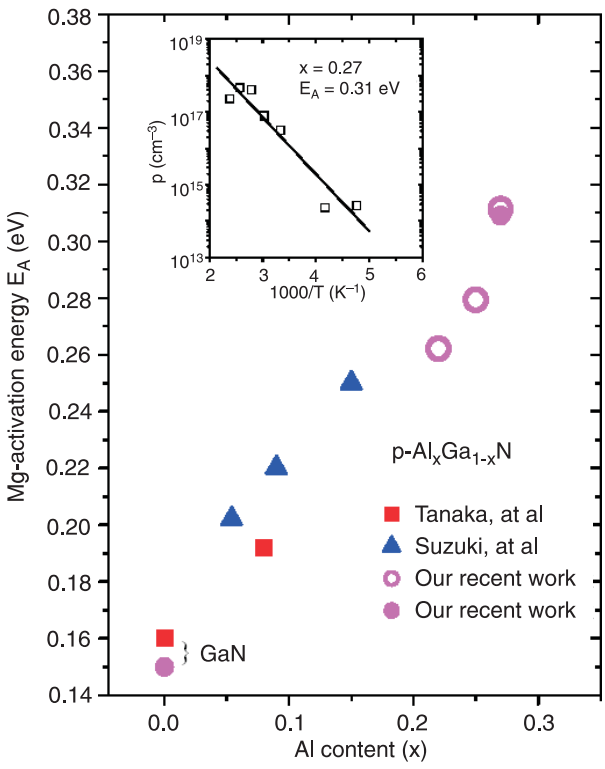

Fig. 8. Activation energy of Mg acceptors in Mg-doped p-type $Al_xGa_{1-x}N$ as a function of Al content x. Closed squares and triangles are data from Refs. 25 and 26 respectively, while closed circles are data from our work, all obtained by Hall measurements. Open circles indicate data obtained from the PL spectra such as those shown in Fig. 7 from our work. The inset shows the measured temperature dependence of the free hole concentration (p) in Mg-doped p-type $Al_{0.27}Ga_{0.73}N$ sample from which E_A = 0.310 eV was obtained (after Ref. 23).

concentration (p) in the Mg-doped p-type $Al_{0.27}Ga_{0.73}N$ sample is shown in the inset of Fig. 8, from which a value E_A = 0.310 eV was obtained. Since the hole concentrations in AlGaN alloys are relatively low and impurity band formation is not likely, our results of E_A deduced from the PL spectra match quite well with those obtained by Hall measurements, which further corroborates our assignment that the observed transitions between 3.62–3.68 eV in Fig. 7 are band-to-impurity transitions of free electrons to the neutral Mg acceptors. The results shown in the inset of Fig. 8 demonstrated conclusively that we have obtained p-type $Al_xGa_{1-x}N$ epilayers with x up to 0.27. A hole concentration of about 7×10^{16} cm^{-3} and mobility 3 cm^2/Vs at room temperature have been achieved in Mg-doped $Al_{0.27}Ga_{0.73}N$ epilayers.

The increase of E_A with increase in band gap energy for the III-nitrides has been reported previously in other studies [25–27] and is predicted by the effective mass theory [28–30]. As a comparison with our results, the value of E_A estimated from the effective mass theory for x = 0.25 for example, is between 0.263 and 0.294 eV which agrees well with the measured value of 0.279 eV. From the measured E_A versus x in Mg-doped p-type $Al_xGa_{1-x}N$, the resistivity versus x can be estimated as follows:

$$\begin{aligned}\rho(Al_xGa_{1-x}N) &= \rho_o \exp(E_A/kT) = \\ &= \rho_o \exp\{[E_A(GaN) + \Delta E_A]/kT\} = \\ &= \rho(GaN)\{\exp(\Delta E_A/kT)\}\end{aligned} \qquad (3)$$

where $E_A = E_A(Al_xGa_{1-x}N) - E_A(GaN)$ and our p-type GaN has typical resistivity, ρ(GaN), of about 1.0 Ω cm. From Eq. (3), the resistivity of $Al_xGa_{1-x}N$ alloys with higher values of x can be deduced. For example, if the trend in Fig. 8 holds for higher x, at Al content x = 0.45, the activation energy E_A is estimated to be 0.4 eV and the estimated resistivity should be as high as 2.2×10^4 Ω cm. This deepening of the Mg activation energy with Al content presents a real challenge for obtaining p-type AlGaN with high Al contents. Our results thus indicate that alternative methods for acceptor activation in AlGaN alloys with high Al contents have to be developed.

3.4. Optical properties of Al-rich AlGaN/GaN heterostructures

Most recently, we have investigated the growth of $Al_xGa_{1-x}N$/GaN heterostructures with high Al contents.

The transport properties of Al-rich AlGaN/GaN HFET structures have been studied by varying the growth conditions and structural parameters, including Si-doped AlGaN barrier thickness, i-AlGaN spacer layer thickness, and Si doping concentration. It was shown that AlGaN/GaN HFET structures with high Al-contents could supply higher sheet densities (around 10^{14} cm^{-2} at room temperature). These HFET structures may have the potential for many applications in high power electronic devices with high temperature stability.

Optical properties related to two-dimensional electron gas (2DEG) in $Al_xGa_{1-x}As$/GaAs heterostructures have been well studied [5–7]. A photoluminescence (PL) peak related to 2DEG in $Al_xGa_{1-x}As$/GaAs (x = 0.6) heterostructures, the H band, was observable only at low temperatures (T < 20 K) [31–33]. On the contrary, we expect to observe the PL emission line associated with the 2DEG in $Al_xGa_{1-x}N$/GaN heterostructures, particularly in high Al content $Al_xGa_{1-x}N$/GaN heterostructures, at higher temperatures (T > 20 K) because of the strong piezoelectric field near the heterointerface as well as the strong carrier confinement resulting from the large band offset of $Al_xGa_{1-x}N$/GaN heterostructures. However, very few studies have been carried out for the $Al_xGa_{1-x}N$/GaN system [34,35]. In fact, the H band has been recently observed up to 60 K in $Al_xGa_{1-x}N$/GaN (x = 0.22) heterostructures [34].

We have carried out the investigations on the optical properties of $Al_xGa_{1-x}N$/GaN heterostructures with high Al contents [36]. Figure 9 shows the PL spectra of an $Al_{0.5}Ga_{0.5}N$/GaN heterostructure sample with an $Al_{0.5}Ga_{0.5}N$ barrier thickness d = 110 Å measured at different temperatures from 10 to 300 K. The emission line at 3.393 eV (10 K) is attributed to the recombination between the 2DEG and photoexcited holes [36]. Although the peak po-

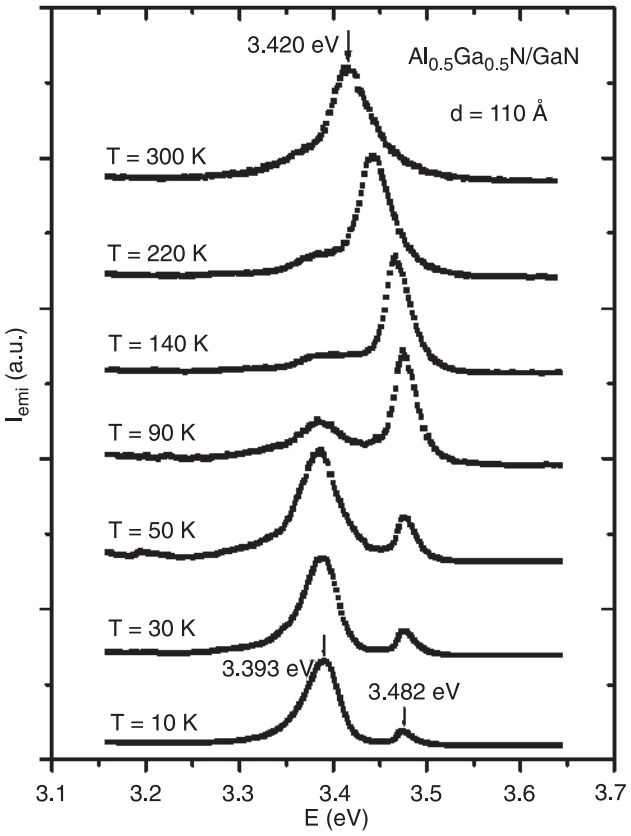

Fig. 9. PL spectra of a representative $Al_{0.5}Ga_{0.5}N$/GaN heterostructure with $Al_{0.5}Ga_{0.5}N$ barrier thickness d = 110 Å measured at different temperatures from 10 to 300 K (after Ref. 36).

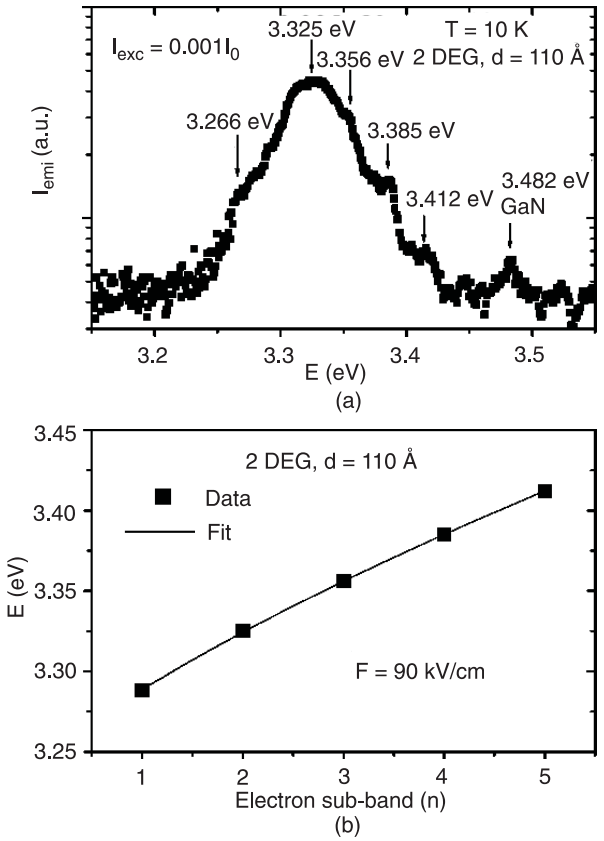

Fig. 10. Low-temperature (10 K) PL spectrum of an $Al_{0.5}Ga_{0.5}N/GaN$ heterostructure under low excitation intensity (10 W/cm^2) and five emission peaks are resolved (a). The least squares fit (solid line) of the observed five emission peak positions (solid squares) with Eq. (3) (b). The fitted value of the total electric field is indicated in the figure (after Ref. 36).

sitions of both 2DEG and the I_2 lines at 3.482 eV (at 10 K) are redshifted with increasing temperature, the energy separation between the 2DEG PL peak and GaN I_2 peak tends to decrease with increasing temperature, which is consistent with a previous observation in low Al content (x = 0.22) $Al_xGa_{1-x}N/GaN$ heterostructures (T ≤ 60 K) [34]. It is striking that the PL emission associated with the 2DEG in $Al_xGa_{1-x}N/GaN$ (x = 0.5) heterostructures is observable even at 220 K, while the 2DEG emission line in $Al_xGa_{1-x}As/GaAs$ (x = 0.6) heterostructures diminishes at temperatures greater than 20 K [31]. This result reflects the fact that $Al_xGa_{1-x}N/GaN$ heterostructures have stronger piezoelectric polarisations as well as much deeper triangular potentials than $Al_xGa_{1-x}As/GaAs$ heterostructures, resulting from larger band offsets and lattice mismatches of $Al_xGa_{1-x}N/GaN$ heterostructures.

Figure 10(a) shows a PL emission spectrum of the $Al_{0.5}Ga_{0.5}N/GaN$ (d = 110 Å) heterostructure under a low intensity excitation I_{exc} (I_{exc} = 10 W/cm^2) measured at 10 K. Five emission lines were observed at emission energies 70, 97, 126, 157, and 216 meV below the GaN I_2 peak (3.482 eV). These emission lines are due to the recombination between 2DEG electrons in different sub-levels and photoexcited holes in the valence band. The solid line in Fig. 10 (b) is the least squares fit of five emission energy peak positions with equation [37]

$$E = \left(\frac{\hbar^2}{2m}\right)\left(\frac{3\pi eF}{2}\left(n+\frac{3}{4}\right)\right)^{2/3} + c, \quad n = 1, 2, \ldots \qquad (4)$$

where m is the electron effective mass, F is the total electric field in the triangular potential well of $Al_xGa_{1-x}N/GaN$ heterostructures, n is the index of the sub-band for electrons, and c is a constant which is determined by the energy gap of GaN as well as the total band bending. The magnitude of piezoelectric field has been measured to be around 0.5 MV/cm for $Al_xGa_{1-x}N/GaN$ (x ~ 0.25) heterostructures [38–40]. The fitted value of 90 kV/cm for this sample seems too low for the total electric field in the triangular potential in $Al_xGa_{1-x}N/GaN$ heterostructures, which we believe is due to the screening of the electrons. The screening electrons are transferred from the Si doped AlGaN barrier layer to the well of $Al_xGa_{1-x}N/GaN$ heterostructures. The Hall effect measurement results revealed that the 2DEG sheet densities in this set of $Al_{0.5}Ga_{0.5}N/GaN$ heterostructure samples were very high, around 1.0×10^{14} cm^{-2}, which corroborates our charge screening explanation.

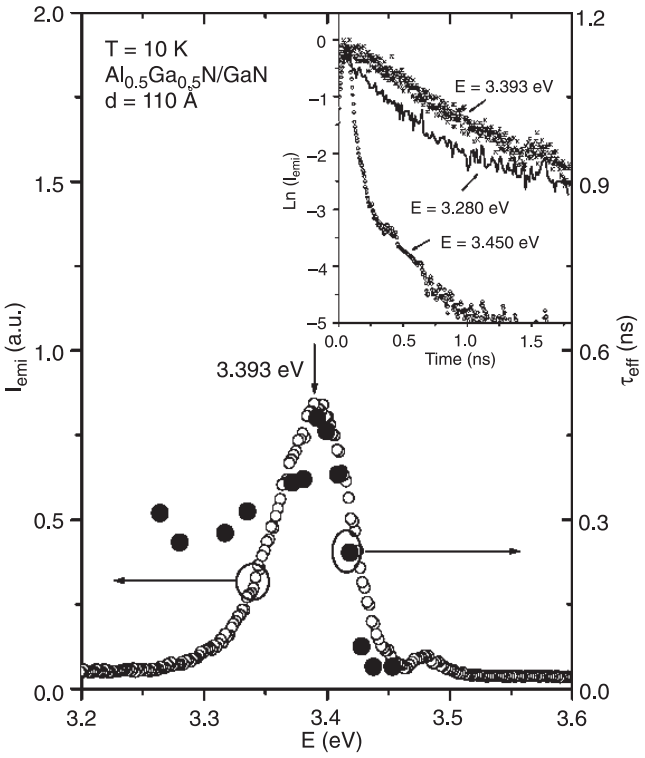

Fig. 11. Emission energy dependence of the decay lifetime of the 2DEG emission line in an $Al_{0.5}Ga_{0.5}N/GaN$ heterostructures sample measured at 10 K. The time-integrated emission spectrum is also shown. The inset shows the temporal responses of the PL emission measured at several different emission energies, which reveal that the decay kinetics can be well described by single exponential functions (after Ref. 36).

The recombination lifetimes were also measured. The inset of Fig. 11 shows the temporal responses of the PL emission measured at several different emission energies, which reveal that the decay kinetics can be well described by single exponential functions, from which the PL decay lifetime can be deduced. Figure 11 shows the low temperature (10 K) PL decay lifetime measured under high laser excitation (10^4 W/cm^2) as a function of emission energy for the 2DEG emission line in $Al_xGa_{1-x}N$/GaN (x = 0.5) heterostructures. A time-integrated PL emission spectrum is also shown. The PL decay lifetime varies between 0.04 and 0.48 ns. At the higher energy side of the emission peak, the decay lifetime increases with an increase in emission energy, which may be due to the fact that the PL decay is dominated by electron transfer from higher sub-bands to lower sub-bands in the triangular wells and the transfer rate is expected to increase with increasing energy. Furthermore, the spatial separation between the recombining electrons in the triangular wells and photoexcited holes is expected to decrease for higher sub-bands, which could also contribute to the observed decay lifetime behaviour.

3.5. Optoelectronic properties of InAlGaN quaternary alloys

By varying In and Al compositions x and y in $In_xAl_yGa_{1-x-y}N$, one can change the energy band gap while keep lattice matched with GaN. In addition to the key features of lattice-match with GaN and the tunability in energy bandgap, $In_xAl_yGa_{1-x-y}N$ quaternary alloys also have the potential to provide a better thermal match to GaN, which could be an important advantage in epitaxial growth. For lattice matching with GaN, the ratio of the concentration of In: Al can be estimated from the formula

$$\begin{aligned} &\boldsymbol{a}[In_xAl_yGa_{1-x-y}N] = \\ &= x\boldsymbol{a}_{InN} + y\boldsymbol{a}_{AlN} + (1-x-y)\boldsymbol{a}_{GaN} \end{aligned} \tag{5}$$

This assumes that a solid solution of InN, AlN and GaN are present in the quaternary. Using values of the lattice constant $\boldsymbol{a}_{InN}$ = 3.548 Å, $\boldsymbol{a}_{AlN}$ = 3.112 Å, and $\boldsymbol{a}_{GaN}$ = 3.189 Å, the ratio x:y of the concentration of In:Al is found to be around 1:4.7 for lattice matching with GaN. When this ratio is inserted in the formula for energy gap (E_g), one obtains the following energy gap variation of $In_xAl_yGa_{1-x-y}N$:

$$\begin{aligned} &E_g[In_xAl_{4.7x}Ga_{1-5.7x}N] = \\ &= xE_g(InN) + 4.7xE_g(AlN) + (1-5.7x)E_g(GaN) = \\ &= (3.4 + 10.6x)\ \text{eV} = [3.4,\ 5.3]\ \text{eV} \end{aligned} \tag{6}$$

with $0 < x < 0.18$ and where we have used E_g(InN) = 0.8 eV, E_g(AlN) = 6.2 eV and E_g(GaN) = 3.4 eV. The bowing effects are not included in Eq. (5) since no data is available for the energy gap of InAlGaN quaternary alloys. This

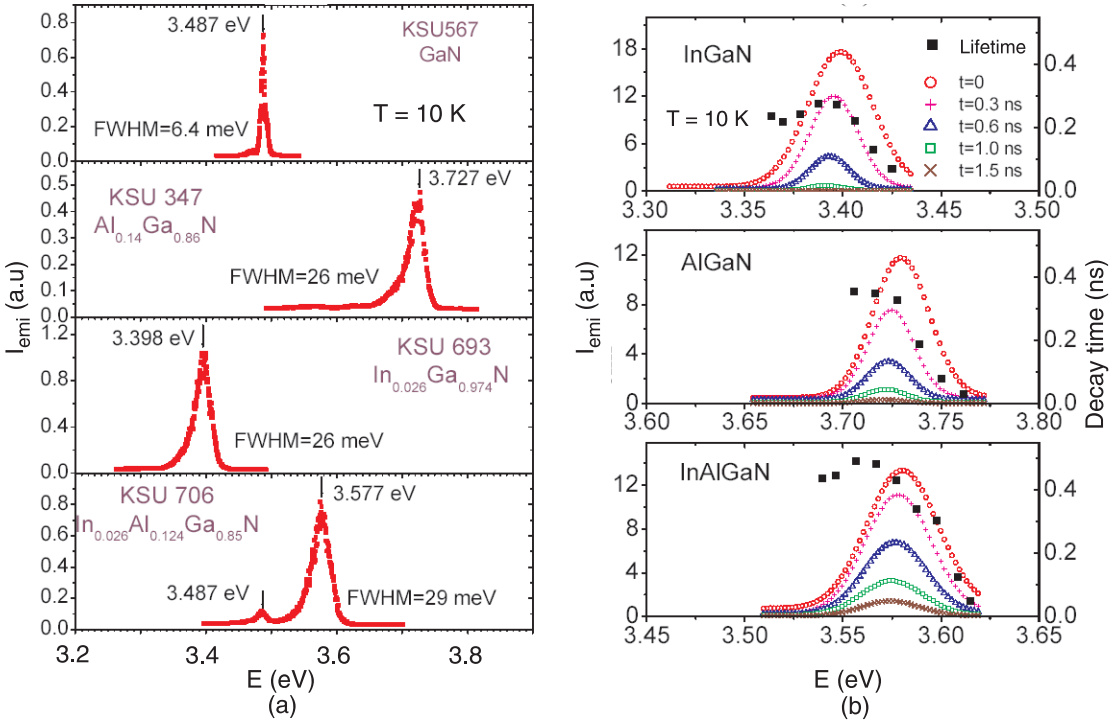

Fig. 12. PL emission spectra of GaN, $Al_xGa_{1-x}N$, $In_xGa_{1-x}N$, and $In_xAl_yGa_{1-x-y}N$ quaternary alloys measured at T = 10 K. The emission spectrum of $In_xAl_yGa_{1-x-y}N$ quaternary alloys shows that we can achieve not only higher emission energies but also higher emission efficiency in InAlGaN quaternary alloys than that of GaN. The emission efficiency of $In_xAl_yGa_{1-x-y}N$ quaternary alloys is also higher than that of $Al_xGa_{1-x}N$ alloy and is comparable to that of $In_xGa_{1-x}N$ alloy (a). Time-resolved PL spectra as well as emission energy dependence of decay lifetime measured at 10 K for $In_xGa_{1-x}N$ alloys, $Al_xGa_{1-x}N$ alloys, and $In_xAl_yGa_{1-x-y}N$ quaternary alloys (b) (after Ref. 41).

indicates the possibility of growing $In_xAl_yGa_{1-x-y}N$ lattice-matched to GaN with band gap energy adjustable from 3.4 to 5.3 eV for deep UV optoelectronic applications.

Our studies have revealed that $In_xAl_yGa_{1-x}N$ quaternary alloys with lattice matched with GaN epilayers ($y \sim 4.7x$) have the highest PL emission intensity as well as the narrowest XRD linewidth [41]. We have also demonstrated that the emission efficiency of the quaternary alloys is about 3 times higher than the AlGaN ternary alloys with a comparable Al content [41]. This is shown in Fig. 12(a), where the PL emission spectra of a typical GaN epilayer (#567), $Al_xGa_{1-x}N$ alloy (#347), $In_xGa_{1-x}N$ alloy (#693), and $In_xAl_yGa_{1-x-y}N$ quaternary alloy (#706) that is lattice-matched to GaN are presented. The arrows indicate the spectral peak positions. The full width at half maximum (FWHM) of each emission line is also included in the figure. The emission spectrum of $In_xAl_yGa_{1-x-y}N$ quaternary alloys in Fig. 12(a) shows that we can achieve not only higher emission energies but also higher emission efficiency in $In_xAl_yGa_{1-x-y}N$ quaternary alloys than that of GaN. The integrated emission intensity of $In_xAl_yGa_{1-x-y}N$ quaternary alloys is higher than that of $Al_xGa_{1-x}N$ alloy of comparable Al content by a factor 3.6 at 300 K and is comparable to that of $In_xGa_{1-x}N$ alloy [41].

Table 2 lists the optimal growth parameters and emission properties of one of the $In_xAl_yGa_{1-x-y}N$ quaternary alloy samples that is lattice matched with GaN together with those of $In_xGa_{1-x}N$ and $Al_xGa_{1-x}N$ alloys. Room temperature electron mobilities and concentrations have also been measured and listed in Table 2 as well. From Table 2, it is interesting to note that the growth conditions as well as the emission properties of $In_xAl_yGa_{1-x-y}N$ quaternary alloys are more closely related with $In_xGa_{1-x}N$ than $Al_xGa_{1-x}N$. The growth temperature and pressure for the optimised $In_xAl_yGa_{1-x-y}N$ quaternary alloys (T_g = 780°C and P = 300 τ) are exactly the same as for $In_xGa_{1-x}N$ alloys. The relative integrated PL emission intensities of $In_xAl_yGa_{1-x-y}N$ quaternary alloys are 175 (T = 10 K) and 2.58 (T = 300 K). These values are comparable with the values of 185 (T = 10 K) and 3.9 (T = 300 K) for InGaN, but much larger than the values of 80 (T = 10 K) and 0.72 (T = 300 K) for AlGaN. It is thus concluded that $In_xAl_yGa_{1-x-y}N$ quaternary alloys are InGaN-like rather than AlGaN-like, although Al composition is almost a factor of 5 larger than In.

The dominant PL transitions in $In_xAl_yGa_{1-x-y}N$ quaternary alloys at low temperatures are also due to the localised exciton recombination, just as the cases in InGaN and AlGaN alloys. This fact is reflected in the characteristics of time-resolved PL as well as decay lifetimes, as shown in Fig. 12(b). The behaviour of emission energy dependence of decay lifetime is very similar among these three alloys. Decay lifetimes of PL emission at their spectral peak positions for InAlGaN, InGaN and AlGaN alloys and are listed in Table 2. While InAlGaN has the longest decay lifetimes, the decay lifetime decreases with an increase in emission energy at energies above their corresponding spectral peak positions. This is a well-known character of localised excitons and is due to the transfer of excitons from higher to lower energy sites within the tail states caused by alloy fluctuations [42]. The increased decay lifetime as well as activation energy in quaternary alloys points to an enhanced localisation effects in $In_xAl_yGa_{1-x-y}N$ quaternary alloys compared with InGaN and AlGaN ternary alloys. The

Table 2. Comparison of InAlGaN quaternary alloys with InGaN and AlGaN (after Ref. 41).

Samples	$In_xGa_{1-x}N$	$Al_xGa_{1-x}N$	$In_xAl_yGa_{1-x-y}N$
Growth parameters: P (Torr) T (°C)	 300 780	 270 1060	 300 780
XRD (002) (arcsec)	359	375	411
In and Al contents	x ~0.026	x ~0.136	x ~0.026, y ~0.124
μ (cm^2/Vs) n (10^{17} cm^{-3})	222 2.50	215 5.40	236 3.60
E_p (eV) T = 10 K T = 300 K	3.395 3.348	3.722 3.674	3.575 3.542
I_{emi} (a.u.) T = 10 K T = 300 K	 185 3.9	 80 0.72	 175 2.58
FWHM (meV)	26	26	29
$E_{activation}$ (meV)	16.3	16.7	23.4
τ (ns) (T = 10 K)	0.28	0.35	0.49

measured PL decay lifetime for $In_xAl_yGa_{1-x-y}N$ quaternary alloys at T = 10 K, from Table 2, is 0.49 ns, while that for InGaN and AlGaN are 0.28 and 0.35 ns, respectively. It is interesting that the measured decay lifetime of $In_xAl_yGa_{1-x-y}N$ quaternary alloys at T = 10 K, $\tau_{InAlGaN,}$ is correlated with those of InGaN and AlGaN alloys, τ_{InGaN} and $\tau_{AlGaN,}$ through the relation $\tau_{InAlGaN}$ (= 0.49 ns) $\approx (\tau^2_{InGaN} + \tau^2_{AlGaN})^{1/2} = (0.28^2 + 0.35^2)^{1/2} = 0.45$ ns. This fact provides some hint that localisation effects in $In_xAl_yGa_{1-x-y}N$ quaternary alloys are the summation of those in AlGaN and InGaN alloys with comparable In and Al compositions. Further evidence to support this speculation is that the relation between the activation energies, E_0, in $In_xAl_yGa_{1-x-y}N$ quaternary alloys and InGaN and AlGaN ternary alloys as shown in Table 2 is the same as the decay lifetimes, i.e., $E_{0,InAlGaN} = 23.4$ meV $\approx (E^2_{0,AlGaN} + E^2_{0,InGaN})^{1/2} = (16.3^2 + 16.7^2)^{1/2}$ meV = 23.3 meV.

We have also fabricated UV photoconductive detectors based on $In_xAl_yGa_{1-x-y}N$/GaN quaternary alloy heterostructures [43]. As shown in Fig. 13, we found that with varying In and Al compositions, the cut-off wavelength of the $In_xAl_yGa_{1-x-y}N$ detectors could be varied to the deep UV range and that the responsivity of the $In_xAl_yGa_{1-x-y}N$ quaternary alloys exceeded that of AlGaN alloys with comparable cut-off wavelengths by a factor of five [43]. We therefore believe that quaternary materials open a new avenue for the fabrication of high efficient UV light emitters as well as detectors.

The important implication of our results is that not only $In_xAl_yGa_{1-x-y}N$ quaternary alloys can provide lattice match with GaN, but also the quantum efficiency (QE) of $In_xAl_yGa_{1-x-y}N$ quaternary alloys is also much higher than that of AlGaN with a comparable Al composition. The enhanced QE have been observed recently in unstrained InGaN/InAlGaN QWs and was attributed to the reduction of dislocation density as well as of the piezoelectric field [44]. Our results show that besides the advantages of reducing dislocation density and/or piezoelectric field in lattice-matched InGaN/InAlGaN and GaN/InAlGaN QWs, QE of InAlGaN is also higher than that of AlGaN with a comparable Al composition. This makes the InAlGaN quaternary alloys a better choice for many UV optoelectronic applications over AlGaN. It is expected that detrimental effects due to lattice mismatch between the barrier and well materials, such as layer cracking, piezoelectric field, and high dislocation density will be significantly reduced in devices based on quaternary alloys compared with those utilising ternary alloys. This is very important for UV emitter applications, where either AlGaN or InAlGaN will be used as active layers. The possible physics involved here is probably very similar with that between GaN and InGaN. It has been well established that emission intensity in InGaN alloys is much higher than that of GaN epilayers due to the effects of carrier localisation in In-rich nanostructures [45]. It is thus not surprising that emission intensity of InAlGaN is higher than that of AlGaN, attributed probably again to the inherent properties associated with the presence of In.

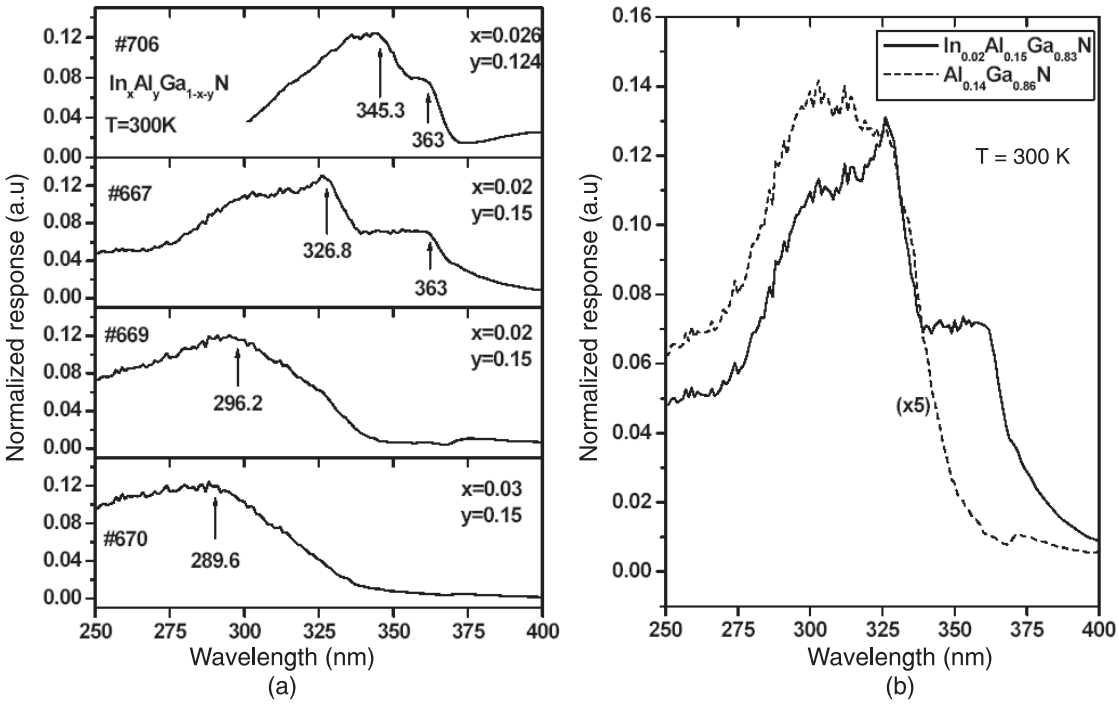

Fig. 13. Normalised photoresponse versus excitation wavelength of $In_xAl_yGa_{1-x-y}N$ quaternary alloys with different In and Al contents. The arrows indicate the cut-off wavelength for the quaternary alloys. The photoresponse from the underlying GaN epilayer in the two samples #706 and #667 is seen as the steps at 363 nm (a). The response of $In_xAl_yGa_{1-x-y}N$ quaternary alloy (solid line) and $Al_yGa_{1-y}N$ alloy (dotted line) with comparable cut-off wavelength. The compositions for these samples are estimated to be $In_{0.02}Al_{0.15}Ga_{0.83}N$ and $Al_{0.14}Ga_{0.86}N$, respectively (b) (after Ref. 43).

3.6. Achieving high optical quality AlN epilayers

Because of our unique optical characterisation capability, recently we have also successfully grown AlN epilayers on sapphire with high optical quality. For the first time, we have produced AlN epilayers that emit band-edge PL transition lines [46]. The 1-μm thick AlN epilayers were grown by metal-organic chemical vapour deposition (MOCVD) on sapphire (0001) substrates with low temperature AlN nucleation layers.

Figure 14(a) compares the low temperature (10 K) PL spectra of our AlN and GaN epilayers covering a broad spectral range from 2.2 to 6.2 eV for AlN and 1.8 to 3.6 eV for GaN. One can see that the peak emission intensity of the deep level impurity related transition at 2.16 eV (the yellow line) in GaN epilayers is about four orders of magnitude lower than that of the band-edge transition at about 3.48 eV, revealing the high optical quality of our GaN epilayers. In AlN, there are two broad emission bands related with deep level impurities at about 2.94 and 4.36 eV, however with peak (integrated) emission intensity being only 1% (3%) of that of the band-edge emission line at 6.033 eV, which indicates that the optical quality of our AlN epilayers is also sufficiently high. It was observed that the optical quality or the intensity ratio of the band-edge to the deep level impurity transitions depends strongly on the growth conditions.

Figure 14(b) compares the room temperature PL spectra of AlN and GaN epilayers, again covering broad spectral ranges. One sees that at room temperature the PL emission intensity of the deep level impurity related transition is also about 2 orders of magnitude lower than that of the band-edge transition in our AlN epilayers. This points to a much-improved optical quality of our AlN epilayers over those in previous cathodoluminescence (CL) studies, in which a comparable peak emission intensity for the deep level impurity related and the band-edge transition lines was observed in AlN grown on sapphire substrates [47,48]. It is interesting to note from Fig. 14 that although the 10 K band-edge emission intensity is about one order of magnitude lower in AlN than in GaN, the room temperature emission intensities are comparable for both compounds. This implies that the thermal quenching of PL emission intensity is greatly reduced in AlN over GaN, which suggests that the detrimental effects of impurities and dislocations or non-radiative recombination channels on the quantum efficiency in AlN is much less severe than in GaN. This points to the great potential of AlN for many device applications, because it is already well known that the detrimental effect of dislocations/impurities in GaN is much smaller than in other III-V and II-VI semiconductors.

In the past, AlN is referred as a ceramic due to its very large bandgap, poor quality, and highly insulating nature and is considered useful as a semiconductor only when alloyed with GaN or used as buffer and spacer layers in nitride structures and devices. Our results show that it is now emerging as an important semiconductor material, namely AlN epilayers of high optical qualities can be achieved by MOCVD. Since it is still at a very early stage for AlN

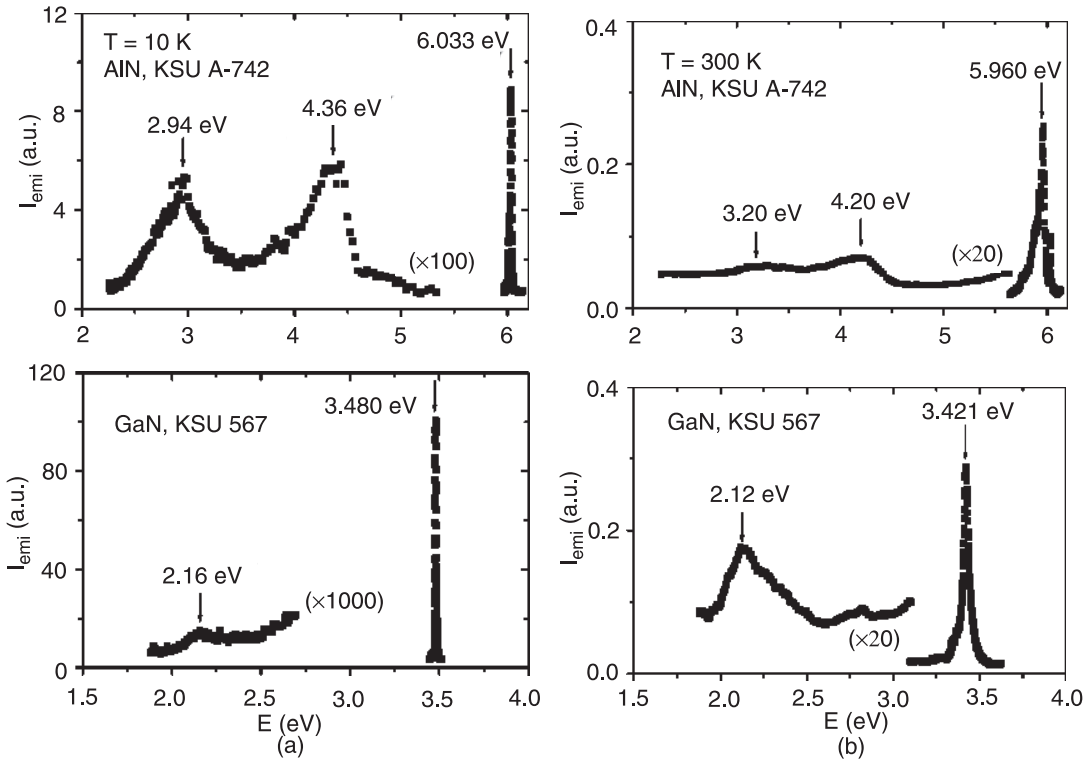

Fig. 14. PL spectra of AlN and GaN epilayers measured at (a) 10 K and (b) 300 K, which cover broad spectral ranges to include both the band-edge and deep level impurity transitions (after Ref. 46).

epilayer growth, significant improvements in materials quality are anticipated. Indeed, it was also shown recently that the conductivity of AlN can be controlled and n-type conduction with a free electron concentration of about 1×10^{17} cm^{-3} has been achieved by Si doping [49]. With the demonstrated abilities of achieving high optical quality here and the n-type conductivity control of AlN epilayers, many novel applications of III-nitrides are conceivable.

3.7. Demonstration of micro-size III-nitride UV light emitters

Recently, our group has successfully fabricated UV (340 nm) micro-size light emitting diodes (LEDs) and arrays based on AlGaN as well as InAlGaN quantum wells (QWs). The LED wafers used were grown on sapphire substrates with 30 nm AlN buffer layers. The AlGaN QW LED layer structure consists of a 0.5 μm of Si-doped n-type $Al_{0.18}Ga_{0.82}N$ ohmic contact layer, 0.5 μm of silicon doped n-type superlattice consisting alternating layers of 50 Å/50 Å of AlN/$Al_{0.2}Ga_{0.8}N$, a 1.0 μm silicon doped n-type $Al_{0.18}Ga_{0.82}N$, a 20 Å undoped $Al_{0.08}Ga_{0.92}N$ active quantum well, a 30 Å of undoped $Al_{0.18}Ga_{0.82}N$ barrier, a 7 nm of Mg doped p-type $Al_{0.27}Ga_{0.73}N$ blocking layer, 0.2 μm superlattice consisting alternating layers of 50 Å /50 Å of AlN/$Al_{0.2}Ga_{0.8}N$, and 0.1 micron Mg-doped GaN p-ohmic contact layer, followed by a rapid thermal anneal at 950°C for 5 seconds in nitrogen. The incorporation of the p-type AlN/AlGaN superlattice structure is to further enhance the p-type conduction, while the insertion of the p-type $Al_{0.27}Ga_{0.73}N$ blocking layer is to ensure the carrier confinement in the well region. InAlGaN QW based UV LED wafers have also been fabricated, in which case InAlGaN QW replaces the active region. Arrays of micro-size UV LEDs with individual disk diameter around 10 microns were then fabricated from the QW LED wafers by photolithography patterning, inductively coupled plasma dry etching, and Ohmic contact metallisation, adapting the technologies established for the blue micro-size emitter fabrication [50–55]. In Fig. 15, optical microscope images of two representative 340 nm micro-size UV LEDs under operation are shown. Figure 15 also compares the electroluminescence (EL) spectra of AlGaN and InAlGaN based 340 nm micro-size UV LEDs. It was found that the spectral line shape of the InAlGaN QW based UV LEDs is much improved over those AlGaN QW based UV LEDs, namely the EL emission from the GaN epilayers at 382 nm is significantly reduced in quaternary LEDs. It was also found that the problems associated with conventional broad-area UV emitters, such as poor current spreading and extraction efficiency, were significantly reduced in quaternary micro-size UV emitters.

The development of micro-size solid-state UV emitter arrays based on III-nitrides would allow chip-scale integration of Chem/Bio sensors for detection of chemical or biological threats. Other applications include pre-cancer cells detection with compact UV source in medical and health. Protein fluorescence is generally excited by UV light sources and changes in intrinsic fluorescence can be used to monitor structural changes in a protein. The availability of chip-scale UV light sources may open new avenues for medical research.

4. Conclusions

As of this writing, rapid progress has been made recently in the area of III-nitride UV emitters. Recently, Professor Asif Khan's group at University of South Carolina has achieved UV LEDs with emission wavelengths shorter than 340 nm and milliwatts output power under pulsed operation [56]. Professor M. Razeghi's group at Northwestern University

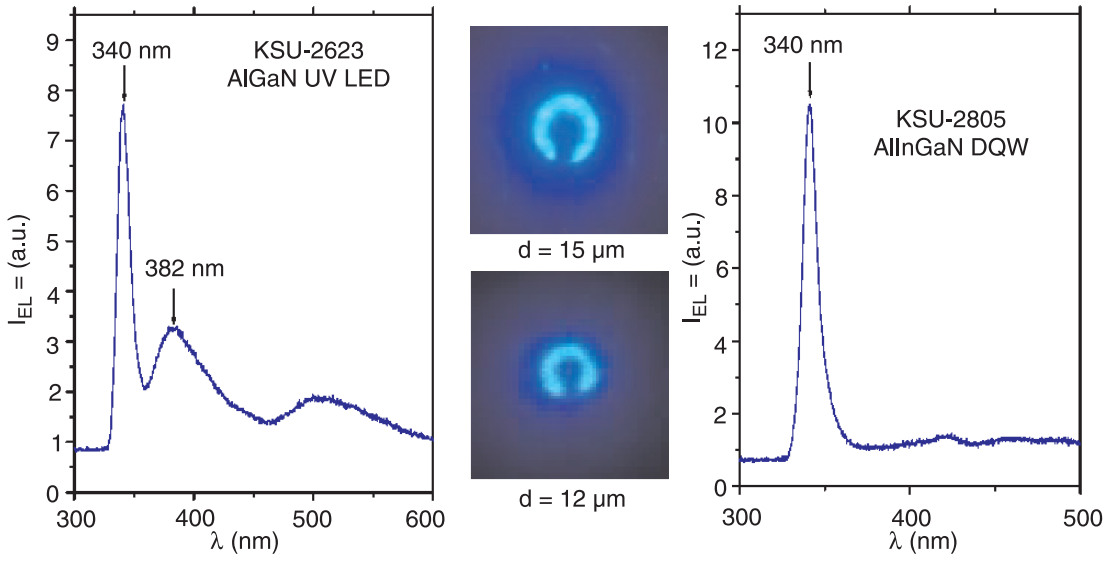

Fig. 15. Comparison of electro-luminescence spectra of 340 nm micro-size UV LEDs fabricated from AlGaN ternary and InAlGaN quaternary alloys. Shown in the centre figure: optical microscope images of 340 nm micro-size UV LEDs with two different sizes under operation.

has demonstrated the operation of a 280 nm UV LED under pulsed operation [57]. Most recently, an InAlGaN quaternary alloy based 348 nm UV LED with 1 mW output power at a cw injection current of 50 mA has been achieved [58]. All these recent results demonstrate that III-nitride materials are very promising for UV photonic device applications. However, there are many problems and questions that still stand in the way of the practical device implementation of deep UV emitters. Methods for improved material qualities as well as doping efficiencies still need to be further explored.

The use of AlN bulk single crystals as substrates are expected to reduce crystal defect densities as well as UV photon absorption in UV emitter structures due to its better lattice constant and thermal expansion coefficient matches over other substrates, high thermal conductivity, and large energy gap. Thus epitaxial growth conditions for UV emitter materials and device structures on AlN bulk substrates have to be optimised. Novel approaches for ohmic contact fabrication, p-type contacts in particular, must be further developed to curtail the problem of very low p-type conductivity in AlGaN alloys with high Al contents. The incorporation of AlGaN or InAlGaN superlattice structures [59,60,52] and tunnel junctions p^{++}/n^{++} [61] are good examples of new approaches for tackling the problem of low p-type conductivities of AlGaN. A better understanding of fundamental properties of AlGaN alloys and their associated QWs with high Al contents is also essential.

In comparison to the recent burgeoning activities in the area of UV emitter materials and device structures, much less effort is devoted to the studies of AlGaN/GaN based HFET structures with high Al contents. The use of high Al-content AlGaN layer is expected to increase the overall figure of merit of the AlGaN/GaN HFETs due to the combined advantages of enhanced band offset and lattice mismatch-induced piezoelectric field, both of which are known to provide higher 2DEG densities in the channel. The growth of $Al_xGa_{1-x}N$/GaN HFET structures with $x = 0.5$ has been reported previously [62]. It was fond that the electron sheet density (and the μn product) was almost the same for $Al_xGa_{1-x}N$/GaN HFET structures with $x = 0.5$ and $x = 0.25$ and the highest achieved room temperature electron sheet density in $Al_{0.5}Ga_{0.5}N$/GaN heterostructures was 1.2×10^{13}/cm^2 with a mobility around 1200 cm^2/Vs. Nevertheless, an improved CW power density was observed in $Al_{0.5}Ga_{0.5}N$/GaN HFETs over those in structures of lower Al contents. The power density was found to increase with Al content. The inability to increase the carrier sheet density with Al content larger than 35% was attributed to the reduced doping efficiency [62]. The difficult to grow high quality AlGaN/GaN HFET structures with high Al contents was attributed partly due to the increased lattice and thermal mismatch between the GaN and AlGaN layers. Our investigations carried out on $Al_{0.5}Ga_{0.5}N$/GaN heterostructures discussed in section 3.4 revealed that these structures represent a very interesting system for studying the fundamental properties of the 2DEG system. Furthermore, our results have shown that a 2DEG sheet density above 10^{14} cm^{-2} can be achieved in $Al_{0.5}Ga_{0.5}N$/GaN heterostructures. Together with the use of special device designs such as gate insulation layers for minimising leakage currents [63–68], high Al content AlGaN/GaN heterostructures could be a very interesting system with the potential for achieving high power performance HFETs.

Acknowledgements

Our research program is supported by grants from DARPA, BMDO, ARO, ONR, DOE, and NSF. This review paper is a collection of contributions from our group members: J. Li, K.H. Kim, K.B. Nam, M.L. Nakarmi, S.X. Jin, T.N. Order, J. Shakya., and Z.Y. Fan.

References

1. S. Nakamura and G. Fasol, *The Blue Laser Diode*, Springer, New York, 1997.
2. H. Morkoc, S. Strite, G.B. Gao, M.E. Lin, B. Sverdlov, and M. Burns, *J. Appl. Phys.* **76**, 1363 (1994).
3. Nitride News, *Compound Semiconductor*, Vol. 3, p. 4, 1997.
4. T. Whitaker, *Compound Semiconductors* **7**, 50 (2001).
5. Gallium Nitride, *Semiconductors and Semimetals*, Vol. 50, volume editors J.I. Pankove and T.D. Moustakas, edited by R.K. Willardson and E.R. Weber, Academic Press 1998.
6. I. Akasaki and H. Amano, *Jpn. J. Appl. Phys.* **36**, 5393 (1997).
7. Y. Sato, N. Takahashi, and S. Sato, *Jpn. J. Appl. Phys.* **35**, L838 (1996).
8. F. Hide, P. Kozodoy, S.P. Denbaars, and A.J. Heeger, *Appl. Phys. Lett.* **70**, 2664 (1997).
9. M.A. Khan, V. Adivarahan, J.P. Zhang, C. Chen, E. Kuokatis, A. Chitnis, M. Shatalov, J.W. Yang, and G. Simin, *Jpn. J. Appl. Phys.* **40**, L1308 (2001).
10. J. Wu, W.W. Walukiewicz, K.M. Yu, J.W. Ager III, E.E. Haller, H. Lu, W.J. Schaffer, Y. Saito, and Y. Nanishi, *Appl. Phys. Lett.* **80**, 3967 (2002).
11. http://www.phys.ksu.edu/area/GaNgroup
12. J. Li, K.B. Nam, J.Y. Lin, and H.X. Jiang, *Appl. Phys. Lett.* **79**, 3245 (2001).
13. *Semiconductors-Basic Data*, 2nd revised edition, edited by Otfried Madelung, Springer, Berlin, 1996.
14. G. Coli, K.K. Bajaj, J. Li, J.Y. Lin, and H.X. Jiang, *Appl. Phys. Lett.* **78**, 1829 (2001) and *Appl. Phys. Lett.* **80**, 2907 (2002).
15. H.S. Kim, R.A. Mair, J. Li, J.Y. Lin, and H.X. Jiang, *Appl. Phys. Lett.* **76**, 1252 (2000).
16. G.D. Chen, M. Smith, J.Y. Lin, H X. Jiang, M. Asif Khan, and C.J. Sun, *Apppl. Phys. Lett.* **67**, 1653 (1995).
17. M.D. Bremser, *Gallium Nitride and Related Semiconductors*, edited by J.H. Edgar, S. Strite, I. Akssaki, H. Amano, and C. Wetzel, p. 147.
18. K.B. Nam, J. Li, M.L. Nakarmi, J.Y. Lin, and H.X. Jiang, *Appl. Phys. Lett.* **81**, 1038 (2002).
19. X. Zhang, S.J. Chua, W. Liu, and K.B. Chong, *Appl. Phys. Lett.* **72**, 1890 (1998).
20. Z.Q. Li, H. Chen, H.F. Liu, L. Wan, M.H. Zhang, Q. Juang, and J.M. Zhou, *Appl. Phys. Lett.* **76**, 3765 (2000).

21. S. Ruvimov, Z. Liliental-Weber, T. Suski, J.W. Ager III, and J. Washbum, *Appl. Phys. Lett.* **69**, 990 (1996)
22. K.C. Zeng, J.Y. Lin, H.X. Jiang, A. Salvador, G. Popovici, H. Tang, W. Kim, and H. Morkoc, *Appl. Phys. Lett.* **71**, 1368 (1997).
23. J. Li, T.N. Oder, M.L. Nakarmi, J.Y. Lin, and H.X. Jiang, *Appl. Phys. Lett.* **80**, 1210 (2002).
24. Y. Koide, H. Itoh, M.R.H. Khan, K. Hiramato, N. Sawaki, and I. Akasaki, *J. Appl. Phys.* **61**, 4540 (1987).
25. T. Tanaka, A. Watanabe, H. Amano, Y. Kobayashi, I. Akasaki, S. Yamazaki, and M. Koike, *Appl. Phys. Lett.* **65**, 593 (1994).
26. M. Suzuki, J. Nishio, M. Onomura, and C. Hongo, *J. Cryst. Growth* **189/190**, 511 (1998).
27. K. Kumakura, T. Makimoto, and N. Kobayashi, *Jpn. J. Appl. Phys.* **39**, L337 (2000).
28. I. Akasaki and H. Amano, *Jpn. J. Appl. Phys.* **36**, 5393 (1997).
29. J.B. Xia, K.W. Cheah, X.L. Wang, D.Z. Sun, and M.Y. Kong, *Phys. Rev.* **B59**, 10119 (1999).
30. F. Mireles and S.E. Ulloa, *Phys. Rev.* **B58**, 3879 (1998).
31. Y.R. Yuan, M.A.A. Pudensi, G.A. Vawter, and J.L. Merz, *J. Appl. Phys.* **58**, 397 (1985).
32. J.P. Bergman, Q.X. Zhao, P.O. Holtz, and B. Monemar, *Phys. Rev.* **B43**, 4771 (1991).
33. W. Li, Z. Wang, A. Song, J. Liang, B. Xu, Z. Zhu, W. Zheng, Q. Liao, and B. Yang, *J. Appl. Phys.* **78**, 539 (1995).
34. B. Shen, T. Someya, O. Moriwaki, and Y. Arakawa, *Appl. Phys. Lett.* **76**, 679 (2000).
35. J.P. Bergman, T. Lundström, B. Monemar, H. Amano, and I. Akasaki, *Appl. Phys. Lett.* **69**, 3456 (1996).
36. K.B. Nam, J. Li, M.L. Nakarmi, J.Y. Lin and H.X. Jiang, *Appl. Phys. Lett.* **81**, 1809 (2002).
37. C. Weisbuch and B. Vinter, *Quantum Semiconductor Structures*, Academic Press, London, 1991.
38. H.S. Kim, J.Y. Lin, X.H. Jiang, W.W. Chow, A. Botchkarev, and H. Morkoc, *Appl. Phys. Lett.* **73**, 3426 (1998).
39. J.P. Ibbetson, P.T. Fini, K.D. Ness, S.P. DenBaars, J.S. Speck, and U.K. Mishra, *Appl. Phys. Lett.* **77**, 250 (2000).
40. R. Gaska, J.W. Yang, A.D. Bykhovski, M.S. Shur, V.V. Kaminski, and S.M. Soloviov, *Appl. Phys. Lett.* **72**, 64 (1998).
41. J. Li, K.B. Nam, K. Kim, J.Y. Lin, and H.X. Jiang, *Appl. Phys. Lett.* **78**, 61 (2000).
42. R.A. Mair, J.Y. Lin, H.X. Jiang, E.D. Jones, A.A. Allerman, and S.R. Kurtz, *Appl. Phys. Lett.* **76**, 188 (2000).
43. T.N. Oder, J. Li, J.Y. Lin, and H.X. Jiang, *Appl. Phys. Lett.* **77**, 791 (2000).
44. M.E. Aumer, S.F. LeBoeuf, S.M. Bedair, M. Smith, J.Y. Lin, and H.X. Jiang, *Appl. Phys. Lett.* **77**, 821 (2000).
45. S. Nakamura, *Science* **281**, 956 (1998).
46. J. Li, K.B. Nam, M.L. Nakarmi, J.Y. Lin, and H.X. Jiang, *Appl. Phys. Lett.* (in press).
47. F.R.B. Hossain, X. Tang, K. Wongchotigul, and M.G. Spenser, *Proc. SPIE* **2877**, 42 (1996).
48. C.M. Zettering, M. Ostling, K. Wongchotigul, M.G. Spencer, X. Tang, C.I. Harris, N. Ordell, and S.S. Wong, *J. Appl. Phys.* **82**, 2990 (1997).
49. Y. Taniyasu, M. Kasu, and N. Kobayashi, *Appl. Phys. Lett.* **81**, 1255 (2002).
50. S.X. Jin, J. Li, J.Z. Li, J.Y. Lin, and H.X. Jiang, *Appl. Phys. Lett.* **76**, 631 (2000).
51. S.X. Jin, J. Li, J.Y. Lin, and H.X. Jiang, *Appl. Phys. Lett.* **77**, 3236 (2000).
52. H.X. Jiang, S.X. Jin, J. Li, J. Shakya, and J.Y. Lin, *Appl. Phys. Lett.* **78**, 1303 (2001).
53. S.X. Jin, J. Li, J. Shakya, J.Y. Lin, and H.X. Jiang, *Appl. Phys. Lett.* **78**, 3532 (2001).
54. H.X. Jiang and J.Y. Lin, *The Monthly Publication of SPIE-The internal Society for Optical Engineering*, p. 28, July 2001 issue.
55. H.X. Jiang and J.Y. Lin, *III-Vs Review*, June/July 2001 issue.
56. M. Asif Khan, V. Adivarahan, J.P. Zhang, C. Chen, E. Kuokstis, A. Chitnis, M. Shatalov, J.W. Yang, and G. Simin, *Jpn. J. Appl. Phys.* **40**, L1308 (2001).
57. A. Yasan, R. McClintock, K. Mayes, S.R. Darvish, P. Kung, and M. Razeghi, *Appl. Phys. Lett.* **81**, 801 (2002).
58. T. Wang, Y.H. Liu, Y.B. Lee, J.P. Ao, J. Bai, and S. Sakai, *Appl. Phys. Lett.* **81**, Sept. 30 (2002).
59. P. Kozodoy, M. Hansen, S.P. DenBaars, and U.K. Mishra, *Appl. Phys. Lett.* **74**, 3681 (1999).
60. P. Kozodoy, Y.P. Smorchkova, M. Hansen, H. Xing, S.P. DenBaars, and U.K. Mishra, A. W. Saxler, P. Perrin, and W.C. Mitchel, *Appl. Phys. Lett.* **75**, 2444 (1999).
61. S.R. Jeon, Y.H. Song, H.J. Jang, G.M. Yang, S.W. Hwang, and S. J. Son, *Appl. Phys. Lett.* **78**, 3265 (2001).
62. Y.F. Wu, B.P. Keller, P. Fini, S. Keller, T.J. Jenkins, L.T. Kehias, L.T. Kehias, S.P. DenBaars, and U.K. Mishra, *IEEE Electron Device Lett.* **19**, 50 (1998).
63. Y.F. Wu, B.P. Keller, P. Fini, S. Keller, T.J. Jenkins, L.T. Kehias, L.T. Kehias, S.P. DenBaars, and U.K. Mishra, *IEEE Electron Device Lett.* **19**, 50 (1998).
64. M. Asif Khan, X. Hu, G. Sumin, A. Lunev, J. Yang, R. Gaska, and M.S. Shur, *IEEE Electron Device Lett.* **21**, 63 (2000).
65. M. Asif Khan, X. Hu, A. Tarakji, G. Simin, J. Yang, R. Gaska, and M.S. Shur, *Appl. Phys. Lett.* 77, 1339 (2000).
66. E.M. Chumbes, J.A. Smart, T. Prunty, and J.R. Shealy, *IEEE Trans. Electron Devices* **48**, 416 (2001).
67. X. Hu, A. Koudymov, G. Simin, J. Yang, M. Asif Khan, A. Tarakji, M.S. Shur, and R. Gaska, *Appl. Phys. Lett.* **79**, 2832 (2001).
68. D.H. Cho, M. Shimizu, T. Ide, H. Ookita, and H. Okumura, *Jpn. J. Appl. Phys.* **41**, 4481 (2002).

